RESEARCH ARTICLE

Satellite-derived surface temperature and in situ measurement at Solfatara of Pozzuoli (Naples, Italy)

M. Silvestri[1], C. Cardellini[2], G. Chiodini[3], and M. F. Buongiorno[1]

[1]Istituto Nazionale di Geofisica e Vulcanologia, Centro Nazionale Terremoti, Roma, Italy, [2]Dipartimento di Fisica e Geologia, Università di Perugia, Perugia, Italy, [3]Istituto Nazionale di Geofisica e Vulcanologia, Bologna, Italy

Abstract Ground thermal anomalies in volcanic-hydrothermal systems, where the outflow of hot fluids gives rise to fumarolic fields, soil degassing, and hot soils, have, up to now, rarely been investigated by using satellite. Here we report a comparison between surface temperature derived by satellite data and a large data set of measured soil temperatures and CO_2 fluxes for a volcanic-hydrothermal system, the Solfatara of Pozzuoli (Campi Flegrei, Italy). Surface temperatures derived from ASTER (Advanced Spaceborne Thermal Emission and Reflection Radiometer) data are compared with soil temperatures and CO_2 fluxes from four surveys performed in 2003, 2010, and in 2014. The good match between the spatial distributions of computed and measured temperatures suggests the adequacy of satellite data to describe the Solfatara thermal anomaly, while the correspondence between temperatures and CO_2 fluxes, evidences the link between degassing and heating processes. The ASTER derived surface temperatures (14–37°C) are coherent with those measured in the soil (10–97°C at 10 cm depth), considering the effect of the thermal gradients which characterize the degassing area of Solfatara. This study shows that satellite data can be a very powerful tool with which to study surface thermal anomalies, and can provide a supplementary tool to monitor thermal evolution of restless volcanoes.

1. Introduction

Monitoring of the surface temperature of volcanoes is one of the primary targets for the monitoring of active volcanoes by virtue of the very nature of volcanism, which is associated with the transfer of heat to the surface [*Oppenheimer*, 1998]. The remote measurements of surface temperatures by thermal infrared (TIR), and in particular the availability of long-time series of data, may represent an important tool for volcanic surveillance, especially in large and/or dangerous areas and/or areas difficult to access. Infrared observations would allow the characterization of surface temperature fields, in terms of values and their spatial distribution, providing insights into a particular volcano's activity status, impending changes in activity, and subsurface processes generating thermal anomalies.

In this framework, satellite-based TIR remote sensing provides a very powerful tool with which to study surface temperature, providing global coverage and a suitable data frequency (i.e., about 16 day nadir repeat) and high-spatial resolution (i.e., 90 m pixels).

Various satellite instruments have infrared observational functionality with different characteristics in terms of temporal, spatial, and spectral resolution each of which must usually be traded off against each other [*Blackett*, 2013]. Some sensors have been used to monitor active volcanoes including the Meteosat Second Generation—Spinning Enhanced Visible and InfraRed Imager (MSG-SEVIRI), the Advanced Very High-Resolution Radiometer (AVHRR), the Moderate Resolution Imaging Spectroradiometer (MODIS), and the Advanced Spaceborne Thermal Emission and Reflection Radiometer (ASTER) [*Yamaguchi et al.*, 1998]. In particular, the ASTER, with data measured at a higher-spatial resolution, allows in principle detection of even very small-size thermal anomalies that are missed by MODIS [*Vaughan and Hook*, 2006], promising a broader application. In the last decades, satellite TIR remote sensing tools have been particularly applied to study "erupting" volcanoes. Satellite observations considered lava and pyroclastic flows, lava lakes, and lava domes [*Flynn et al.*, 1994; *Harris et al.*, 1998; *Lombardo et al.*, 2004; *Coppola et al.*, 2010; *Oppenheimer and Yirgu*, 2002; *Davies et al.*, 2008; *Hirn et al.*, 2008; *Wright and Pilger*, 2008; *Kaneko et al.*, 2002; *Vaughan and Hook*, 2006; *Carter and Ramsey*, 2009; *Oppenheimer*, 1993; *Trunk and Bernard*, 2008]. Important studies have

been conducted also for understanding how satellite instruments view volcanic thermal features [*Harris and Stevenson*, 1997; *Pieri and Abrams*, 2005; *Kervyn et al.*, 2008; *Buongiorno et al.*, 2013] that may be a precursor to major eruptions.

On the contrary, a lesser number of studies [e.g., *Lagios et al.*, 2007, *Vaughan et al.*, 2010, 2012a, 2012b] considered volcanic-hydrothermal systems that are usually affected by circulation of hot fluids, resulting at the surface in thermal waters, fumarolic fields, and soil degassing with which hot soils are generally associated. The heat flux released from these hydrothermal manifestations is an important, if not the main, term in the total energy budget for the few volcanic systems where it has been measured [*Chiodini et al.*, 2005; *Hurwitz et al.*, 2012; *Caliro et al.*, 2005].

For example, the thermal energy dissipated daily by the degassing process at the Solfatara of Pozzuoli (the most active zone of Campi Flegrei) has been estimated in the order of 100 MW [*Chiodini et al.*, 2005]. Its cumulative amount over the last 30 years is orders of magnitude greater than the elastic energy released during the last large crisis of Campi Flegrei (1983–1984, more than 10,000 earthquakes). Furthermore this advective heat flux is greater than the energy associated with ground deformation (∼2 m of maximum uplift in 1983–1984), and is about 10 times greater than the conductive heat flux over the entire Campi Flegrei caldera [*Chiodini et al.*, 2001, 2005]. A large heating of the system, caused by the arrival of increasing amounts of deep, possibly magmatic, fluids into the hydrothermal system, has been recently highlighted as the possible cause of the ongoing 10 year-long pattern of accelerating ground deformation [*Chiodini et al.*, 2015].

Campi Flegrei caldera is not a unique case, as such large hydrothermal release of heat affects most, if not all, the calderas of the world and particularly those which are restless [*Chiodini et al.*, 2005; *Vilardo et al.*, 2015; *Bloomberg et al.*, 2014]. Furthermore, Solfatara of Pozzuoli is not a unique case of hydrothermal systems where the thermal energy release is associated with the occurrence of anomalous soil CO_2 degassing [*Chiodini et al.* 2005; *Harvey et al.*, 2015; *Bloomberg et al.*, 2014].

In this work, surface temperatures derived from ASTER data are compared with a large data set including 1763 in situ direct measurements of soil temperatures and CO_2 fluxes at the Solfatara of Pozzuoli. In situ measurements refer to data from four surveys performed in June 2003, May 2010, June 2014, and September 2014, chosen among those already available, as they fall in periods which roughly correspond to those for which ASTER data were available. We compared the different data sets in order both to assess the reliability of ASTER satellite-derived surface temperatures and to test the possibility of their use as proxy of the CO_2 fluxes. Finally, the main aim is to investigate the possible use of long time series of satellite TIR data for the remote monitoring of the hydrothermal features of active volcanoes.

2. The Study Area: Solfatara of Pozzuoli

The Solfatara of Pozzuoli volcano is a tuff cone formed about 4 ky BP and belongs to Campi Flegrei (Naples, Italy), a resurgent caldera generated by two main collapses that emplaced the Campanian Ignimbrite (39 ky BP) [*Costa et al.*, 2014 and references therein] and the Neapolitan Yellow Tuff (NYT; 15 ky BP) [*Deino et al.*, 2004] eruptions (Figure 1). The last magmatic activity occurred with the formation of the Monte Nuovo volcano in the 1538.

Campi Flegrei are characterized by recurrent ground deformation episodes (*bradyseism*) that during the uplift phase are accompanied by seismic activity. The major recent uplift episodes occurred in 1969–1972 and in 1982–1984 (3.8 ± 0.2 m total vertical displacement) [*Del Gaudio et al.*, 2010 and references cited therein]. Since 1985 Campi Flegrei has been subsiding, with a few minor uplift events temporally inverting the ground movement, until 2005 when a new uplift phase started. This new uplift phase accelerated and reached a maximum vertical displacement of about 33 cm by October 2015 [http://www.ov.ingv.it/ov/bollettini-mensili-campania/Bollettino_Vulcani_Campani_2015_11.pdf]. This last stage has been accompanied by weak seismicity, by a strong increase in fumarolic activity, and by important compositional variations in the fumarolic effluents, which were interpreted as increased contributions of fluids from a magmatic source [*Chiodini et al.*, 2012, 2015].

Presently, Solfatara of Pozzuoli is the main site of release of magmatic-hydrothermal fluids by diffuse degassing and fumarolic emissions of the emerged portion of Campi Flegrei [e.g., *Chiodini et al.*, 2001, 2005, 2015].
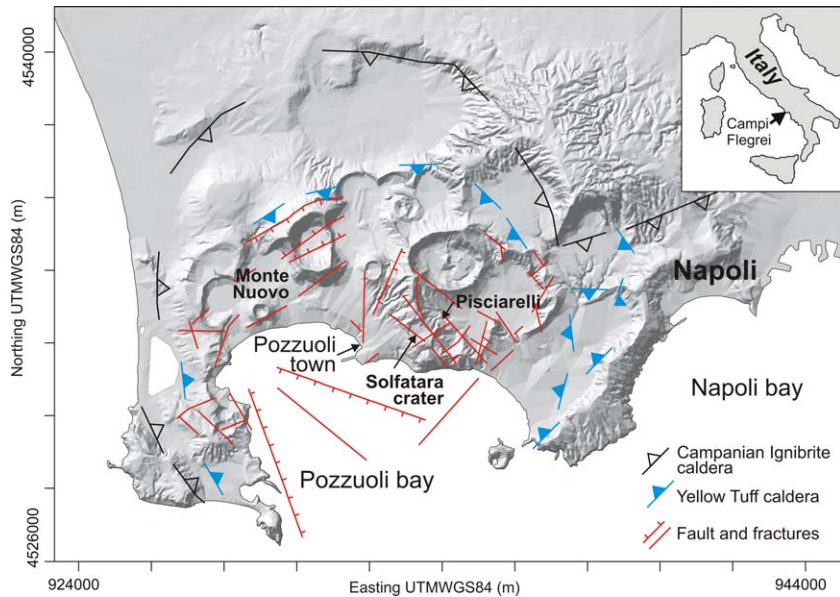
Figure 1. Simplified structural map of Campi Flegrei reporting the location Solfatara of Pozzuoli.

Solfatara is characterized by a large soil diffuse degassing structure (Solfatara DDS) [*Chiodini et al.*, 1998], from where a CO_2 flux, fed by the degassing of the hydrothermal system, is released by the soil in the order of 1000–1500 t/d [*Chiodini et al.*, 2001, 2010; *Cardellini et al.*, 2003]. Solfatara DDS includes not only the area inside the crater (Figure 2) but it extends especially east of the crater, in the Pisciarelli area (Figure 1). Recent measurements showed that fumarolic vents emit an additional amount of 300–800 t/d of volcanic CO_2 [*Aiuppa et al.*, 2013, 2015; *Pedone et al.*, 2014].
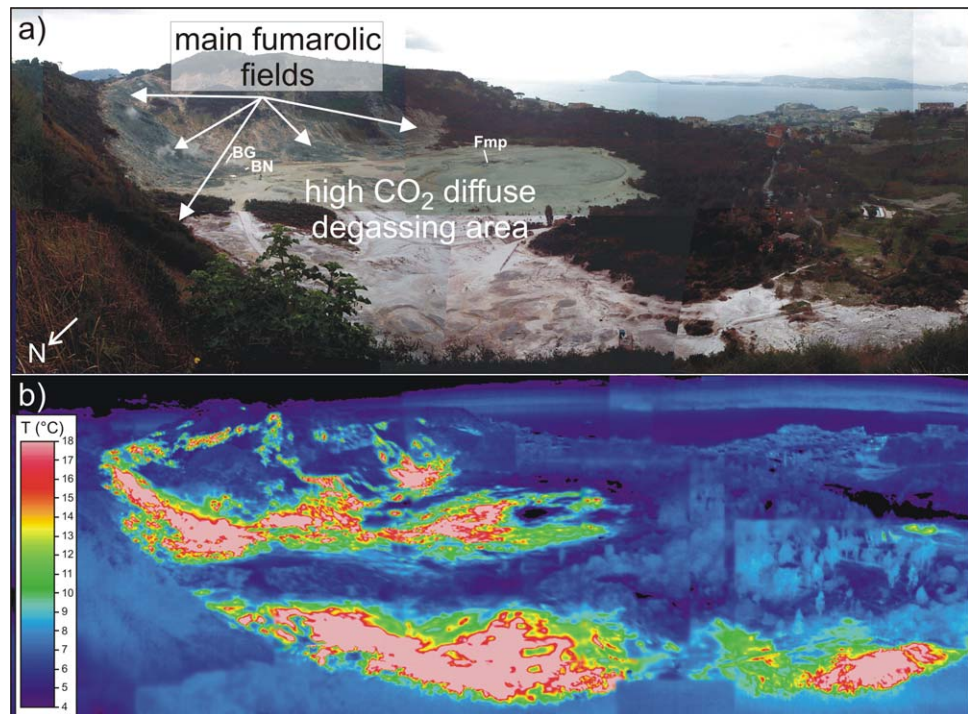

Figure 2. (a) View of the inside of Solfatara crater. The whitish area roughly corresponds to the area with the highest soil CO_2 flux; the mail fumaroles are concentrated along the southern and western borders of the crater plain. The locations of Bocca Grande fumarole (BG), Bocca Nuova Fumarole (BN), and Fangaia mud pool (Fmp) are reported. (b) Infrared image of the same view of the upper plot.

Table 1. ASTER Instrument Characteristics [*Yamaguchi et al.*, 1998]

Instrument	VNIR	SWIR	TIR
Bands and spectral range (μm)	1 0.52–0.60	4 1.60–1.70	10 8.125–8.475
	2 0.63–0.69	5 2.145–2.185	11 8.475–8.825
	3N 0.78–0.86	6 2.185–2.225	12 8.925–9.275
		7 2.235–2.285	13 10.25–10.95
		8 2.295–2.365	14 10.95–11.65
		9 2.360–2.430	
Spatial resolution	15 m	30 m	90 m
Swath width	60 km	60 km	60 km
Cross track pointing	±318 km (±24°)	±116 km (±8.55°)	±116 km (±8.55°)
Quantization (bits)	8	8	12
Revisit time	16 days	16 days	16 days

As pointed out in the work of *Chiodini et al*. [2001], Solfatara DDS is also characterized by anomalous soil temperatures (Figure 2). The correspondence between high CO_2 fluxes and soil temperature has been interpreted as the results of the condensation of the steam originally associated with CO_2. The latent heat of condensation heat the same soils where the CO_2, which is an incondensable gas, is discharged [*Chiodini et al.*, 2005].

Recently, the system has given clear signs of unrest, including the increase of the fumarole temperatures and flow rates [*Chiodini et al.*, 2015; *Aiuppa et al.*, 2015], and the increase of the soil CO_2 fluxes concurrently with a new ground deformation phase and weak seismic activity.

## 3. Data and Methods

3.1. ASTER Satellite Data

The ASTER sensor launched in December 1999 is one of five instruments on the Terra satellite, part of NASA's Earth Observing System (EOS). Terra follows a sun-synchronous nearly polar orbit with an equator crossing time of ∼10:30 A.M./P.M. The ASTER instrument has a 60 km swath width, which allows any point on the surface to be imaged at least once every 16 days. This sensor contains 14 spectral bands including three in the VNIR region (0.5–1.0 μm, with 15 m spatial resolution), six in the shortwave infrared (SWIR) region (1.0–2.5 μm, with 30 m spatial resolution; the SWIR instrument has not been usable since April 2008 because of sensor saturation and severe striping), and five within the thermal infrared (TIR) region (8–12 μm) with 90 m spatial resolution [*Kahle et al.*, 1991] (Table 1).

ASTER is the first orbital sensor that provides publicly available high-spatial resolution data with more than two bands in the TIR region. These data provide the ability to develop new methods for extracting the small scale compositional and temperature structure of the surface [*Ramsey*, 2002; *Carter et al.*, 2009; *Ramsey and Dehn*, 2004].

Since the launch of ASTER in December 1999, 140,000+ images of volcanoes [*Buongiorno et al.*, 2013] have been acquired worldwide with a number of volcanoes seen frequently enough with ASTER at acceptable cloud coverage. Thus, useful time series data analyses can be undertaken. For instance, one such analysis [*Pieri and Abrams*, 2005] detected winter-time summit crater meltwater in advance of an early spring eruption by the subarctic Chikurachki Volcano in the Kurile Islands. ASTER data are currently the only orbital remote sensing data set which allow the detection of low temperature thermal anomalies smaller than the resolution limit of the coarser spatial resolution, MODIS data.

The temperature is not solely an intrinsic property of the surface; beyond the intrinsic geothermal component, it varies with the irradiance history and meteorological conditions. Energy reflected from the surface and clouds adds noise which makes correct interpretation of terrain imaged in the thermal infrared band more difficult. For this study, we have considered the ASTER's night observations because solar heating of the Earth's surface contributes significantly to the total radiant energy flux during the daytime. The night observations show well-defined episodes of increasing thermal emission of the crater contrasting with a more uniform background temperature. Since the launch of the EOS-1 Terra Satellite, more than 35 night cloud-free images have been acquired on the Campi Flegrei area.
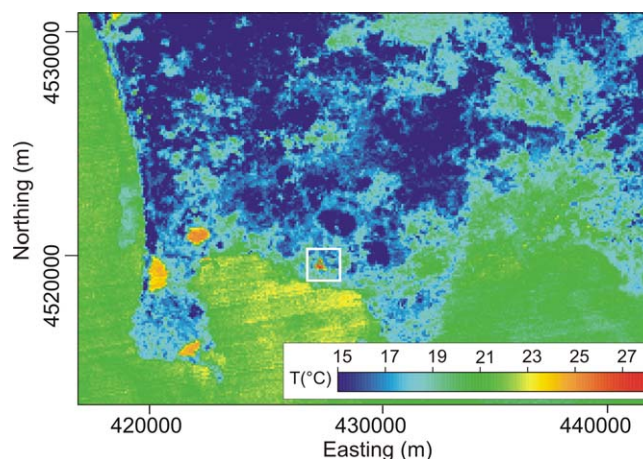
Figure 3. Example of surface temperature derived from ASTER data (26 September 2014 ASTER data set). The white box indicates the area including Solfatara considered in this study within a full ASTER frame.

3.2. ASTER Data Processing Method to Compute Surface Temperatures

The ASTER data product Level-1B data (i.e., radiance at the sensor) has been used because it contains images already resampled to the geometry of the appropriate UTM projection with the WGS84 Datum. In fact the ASTER Level-1B Registered Radiance at the Sensor product contains radiometrically calibrated and geometrically coregistered data for the acquired channels of the three different telescopes of Level-1A data. The Level-1B data set is produced by applying the radiometric calibration and geometric correction coefficients to the Level-1A.

The ASTER data have been processed by means code written in the IDL/ENVI image-processing environment (Exelis Visual Information Solutions, Inc. USA, www.exelisvis.com), implemented in three steps:

1. from the original cloud-free data format (Level-1B), the georeferenced images are obtained using ENVI batch command and the radiance at the sensor is automatically produced;

2. on the ASTER data, the atmospheric correction has been applied in order to remove the effect of the atmosphere. The atmospheric and topographic corrections of remote sensing images are very important to obtain reliable values for many surface parameters (reflectance, vegetation indexes, ocean chlorophyll maps, temperature, etc.) but represent a very difficult preelaboration step. For these data, we have considered the "CIRILLO" atmospheric correction tools [*Musacchio et al.*, 2007]. Information on the atmospheric profiles corresponding in time to the ASTER overflights are provided by University of Wyoming and atmospheric temperature, pressure, and humidity are considered;

3. the TES (Temperature Emissivity Separation) [*Gillespie et al.*, 1998] algorithm for ASTER thermal bands has been used to obtain the surface temperature map (Figure 3). Since the radiance measured by ASTER is a pixel-integrated radiance, that is an area-weighted sum of all the subpixel radiating components, the temperature derived from radiance data by TES is therefore a pixel-integrated temperature considering a homogenous pixel. The effect of inhomogeneous temperature distribution due to the presence of hot spots inside the 90 m ASTER pixel [*Vaughan et al.*, 2010], was not considered in this work due to the features of the possible hot spots at Solfatara. In fact, the major hot spots here are constituted by the main fumaroles (Bocca Grande fumarole, BG; Bocca Nuova fumarole, BN) vent opening and by the Fangaia mud pool (Fmp) (Figure 2), that are characterized by maximum temperatures of $\sim$160°C (BG outlet T $\sim$160°C and BN outlet T $\sim$150°C [*Chiodini et al.*, 2010, 2015]) and 90°C, respectively. Considering that the vent openings of the fumaroles have a maximum spatial extent minor than $\sim$0.09 m^2 (i.e., $\sim$0.001% of the ASTER's 90 m pixels) and a maximum temperature difference with respect to the surrounding soil ($\Delta T_{target-background}$) of $\sim$120°C [e.g., *Chiodini et al.*, 2007], according to the theoretical analysis of *Vaughan et al.* [2010], the temperature of such hot spots cannot be reliably determined. Also the temperature of the Fangaia mud pool area cannot be resolved considering its maximum spatial extent of $\sim$60 m^2 (i.e., $\sim$0.7% of the ASTER's 90 m pixels) and a $\Delta T_{target-background}$ of $\sim$70°C [*Vaughan et al.*, 2010].

The validation of surface temperature obtained by TES was done by comparing the computed temperature with surface temperature measurements, collected during ASTER overflight by an Everest IR thermometer in specific validation field campaigns, performed on July 2003 and October 2009 at Mt. Etna (Italy) and on September 2009 at Solfatara of Pozzuoli [*Buongiorno et al.*, 2008; Agenzia Spaziale Italiana—Sistema Rischio Vulcanico project, ASI-SRV ref ASI I/091/06/0]. In each survey, multiple measurements were performed in different locations over surfaces as compositionally homogeneous as possible in order to minimize spectral heterogeneity. For the Etna survey, an average measured surface temperature of 53 ± 3°C (i.e., average

Table 2. Dates of ASTER Acquisition and Derived Temperatures (T_0) Statistics (Field Survey Dates Are Also Reported)

ASTER Image Date	Field Survey Date	T_0 Min-T_0 Max (°C)	T_0 Mean (T_0 std. dev.) (°C)
24 Jun 2003	01–02 Jul 2003	23.3–36.3	25.9 (1.9)
1 May 2010	17–19 May 2010	14.3–27.7	18.4 (2.1)
22 Jun 2014	6–7 Jun 2014	18.4–29.1	21.6 (1.8)
26 Sep 2014	22–23 Sep 2014	15.3–23.6	17.7 (1.1)

value ± 1 standard deviation), 52 ± 2°C and 36 ± 3°C corresponds to temperatures of 54°C, 50°C, and 32°C derived by TES for the corresponding ASTER pixels. For the Solfatara survey, an average measured surface temperature of 32 ± 3°C corresponds to a temperature of 30°C derived by TES for the corresponding pixel. By comparing these results, we can reasonably assume that the uncertainty of the surface temperatures estimated by TES is generally within 3°C.

3.3. Solfatara of Pozzuoli ASTER Data Sets

Considering the dates of the field surveys dedicated to the soil temperature and soil CO_2 flux measurements from 1998 till 2014, four suitable ASTER data sets were selected to ensure the closest time correspondence between the ASTER pass and the field surveys (Table 2). In Figure 3, an example of a surface temperature map derived by ASTER data is shown. ASTER-derived surface temperature (T_0) extracted from an area of about 1.4 × 1.4 km² including the Solfatara DDS has been considered for the further analyses. The statistical parameters of the T_0 for this area, in the different periods are reported in Table 2.

Considering the spatial resolution of ASTER TIR pixels (90 m) and the selected area, about 196 pixels have been analyzed. As reported in Table 2, surface temperature ranges from a minimum value that can be associated with the background temperature and maximum value related to the most hot pixels including the fumarolic field area where BG and BN fumaroles are located (Figure 4). An example of evidence of a persistent thermal anomaly is also showed in Figure 3, in the white box where the Solfatara area is characterized by temperature higher than the nearby area. By analyzing the surface temperature in Table 2, it is also interesting to note that the minimum and maximum temperatures of the Solfatara of the June 2003 are higher than those of June 2014. This difference is reasonably reflecting the anomalous temperatures of the 2003 summer that was characterized by temperatures 20–30% above the seasonal average over most parts of Europe [*Francis et al.*, 2011; *De Bono et al.*, 2004].
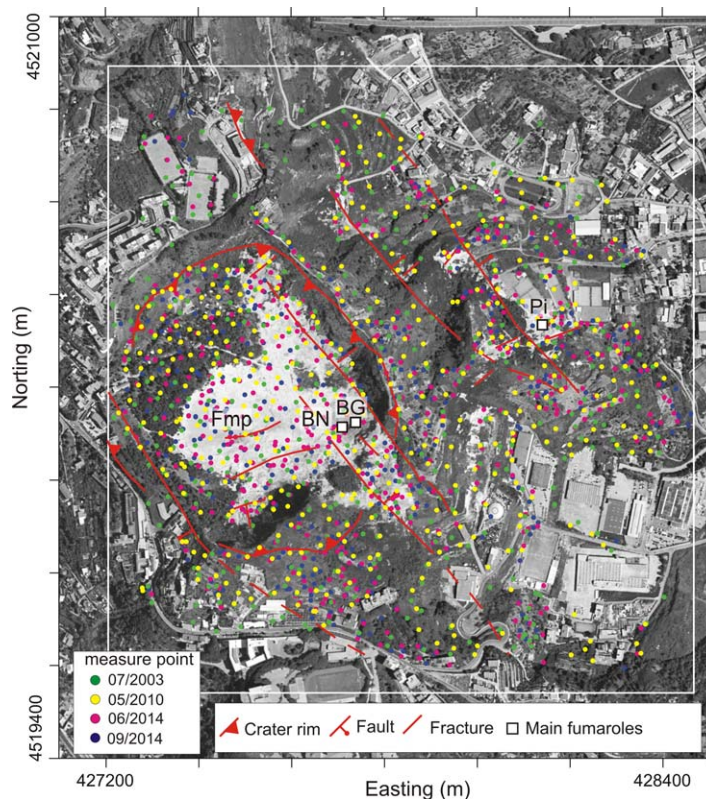
Figure 4. Distribution of CO_2 flux and soil temperature measurements in the four surveys considered in this study. In the figure are also reported the main volcanic and tectonic structures, the location of Fangaia mud pool (Fmp), and the location of the main fumarolic vents: Bocca nuova (BN), Bocca Grande (BG), and Pisciarelli (Pi). The area inside the rectangle is that considered for the mapping of fluxes and temperatures.

3.4. Soil Temperature and CO_2 Fluxes: Measurement and Analysis Methods

Specific surveys devoted to the measurement of soil CO_2 fluxes and soil temperature have been carried out at Solfatara since

Table 3. Statistical Parameters of Measured CO_2 Flux and Soil Temperature

Date	Measure n.	CO_2 Flux Min. (g m^{-2} d^{-1})	CO_2 Flux Max. (g m^{-2} d^{-1})	CO_2 Flux Mean (g m^{-2} d^{-1})	T_{10} Min. (°C)	T_{10} Max. (°C)	T_{10} Mean (°C)
Jul 2003	391	3.8	12823	647	24.3	96.5	38.5
May 2010	505	3.4	35462	875	9.8	94.9	28.8
Jun 2014	468	10.5	27066	1224	21.2	93.4	36.0
Sep 2014	399	3.1	25774	1487	16.3	95.0	32.8

1998 in the framework of the volcanic surveillance of Campi Flegrei and/or of various research projects [e.g., *Acocella and Chiodini*, 2015]. Each survey included the measurement of both parameters in about 400 points randomly distributed (average spacing of the measurements ∼50 m) inside the Solfatara crater area and in its surroundings (Figure 4), especially extending eastward to the Pisciarelli area that is the main degassing area outside the crater.

CO_2 flux measurements were performed using the "accumulation chamber" method which is based on the measurement of the CO_2 concentration increase with time in an inverted chamber placed on the ground [*Chiodini et al.*, 1996, 1998, 2001; *Cardellini et al.*, 2003]. The measurements were carried out using an instrument equipped with a LICOR Li-820 infrared sensor to measure the CO_2 concentrations, operating in the range 0–20,000 ppm of CO_2, and an accumulation chamber with a volume of ∼2.8 L.

Soil temperatures were measured at a depth of 10 cm (T_{10}) using a thermocouple sensor equipped with a rigid probe, at the same locations as the CO_2 flux measurements, accordingly with a routinely used method [e.g., *Chiodini et al.*, 2001, 2005, 2015; *Bergfeld et al.*, 2012; *Bloomberg et al.*, 2014].

In this work, the values of soil CO_2 flux and T_{10} obtained in four surveys, performed in 2003, 2010, and in 2014 are analyzed and discussed (Table 3). These data sets have been chosen, from those already available, to have a time delay as short as possible between ASTER image acquisition and field data (Table 2). The statistical parameters of the measured CO_2 fluxes and T_{10} are reported in Table 3.

Measured soil CO_2 flux values distribute over a wide range, from a few g m^{-2} d^{-1} to 10^4 g m^{-2} d^{-1}, due to the occurrence of multiple gas sources such as the biological activity in the soil (i.e., the root respiration of plants and the decomposition of organic matter, *cfr*. background CO_2 flux) and the degassing of the hydrothermal system [e.g., *Chiodini et al.*, 2001; *Cardellini et al.*, 2003].

In order to obtain maps of CO_2 flux and T_{10} distribution, the measured values of each survey were first elaborated with the approach proposed by *Cardellini et al.* [2003] based on sequential Gaussian simulations (sGs). The sGs method consists of the production of numerous realizations of the spatial distribution of an attribute (CO_2 flux T_{10} this study) here performed using the *sgsim* algorithm described by *Deutsch and Journel* [1998]. Since the sGs assumes multigaussian distribution of the attribute, implying first a distribution of observed values, both CO_2 flux and T_{10} values were transformed into a normal distribution (n-scores of data) using normal-score method (i.e., *nscore* algorithm by *Deutsch and Journel*, [1998]). The transformation consists of substituting the original values of the attribute with those of the corresponding quantiles of a standard normal distribution. The n-scores are then used in the simulation procedure and transformed back into values expressed in original data unit, applying the inverse of the normal score transform, at the end of the simulation process [*Deutsch and Journel*, 1998; *Cardellini et al.*, 2003]. The attribute values are simulated at locations defined by a regular grid. The simulation is conditional and sequential, i.e., n-scores are simulated at each unsampled location by random sampling of a Gaussian conditional cumulative distribution function defined at each location on the basis of original data and of previously simulated data within its neighborhood. Due to the multigaussian assumption, mean and variance of the Gaussian conditional cumulative distribution function is defined at each location as the simple kriging estimate and variance respectively [*Goovaerts*, 1997; *Deutsch and Journel*, 1998]. Simple kriging estimate and variance are computed according to the variogram model of n-scores which define the spatial correlation among the data. The variogram model is defined fitting the experimental variogram of n-scores with a function that needs to obey to certain numerical properties in order for the sGs equations (or other simulation/estimation algorithms) to be solvable [*Isaaks and Srivastava*, 1989].
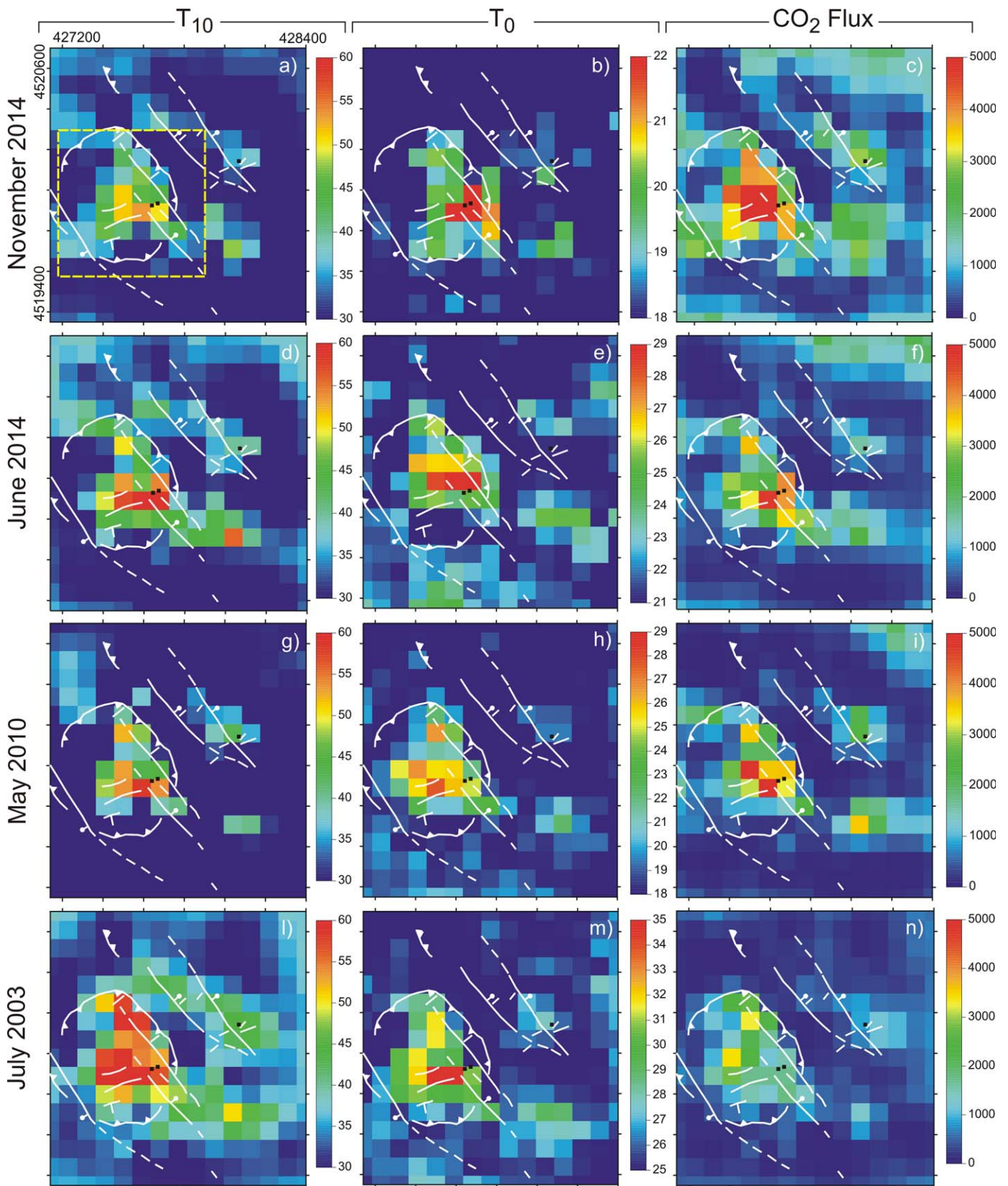
Figure 5. (left) Maps of measured soil temperature, T_{10}, (middle) ASTER-derived surface temperature, T_0, and (right) measured CO_2 flux for each survey. In the maps are reported the main volcanic-tectonic structure and the main fumaroles (see Figure 4). In (a) the box including the Solfatara crater area (see Figure 7–9) is also reported with a dashed yellow line.
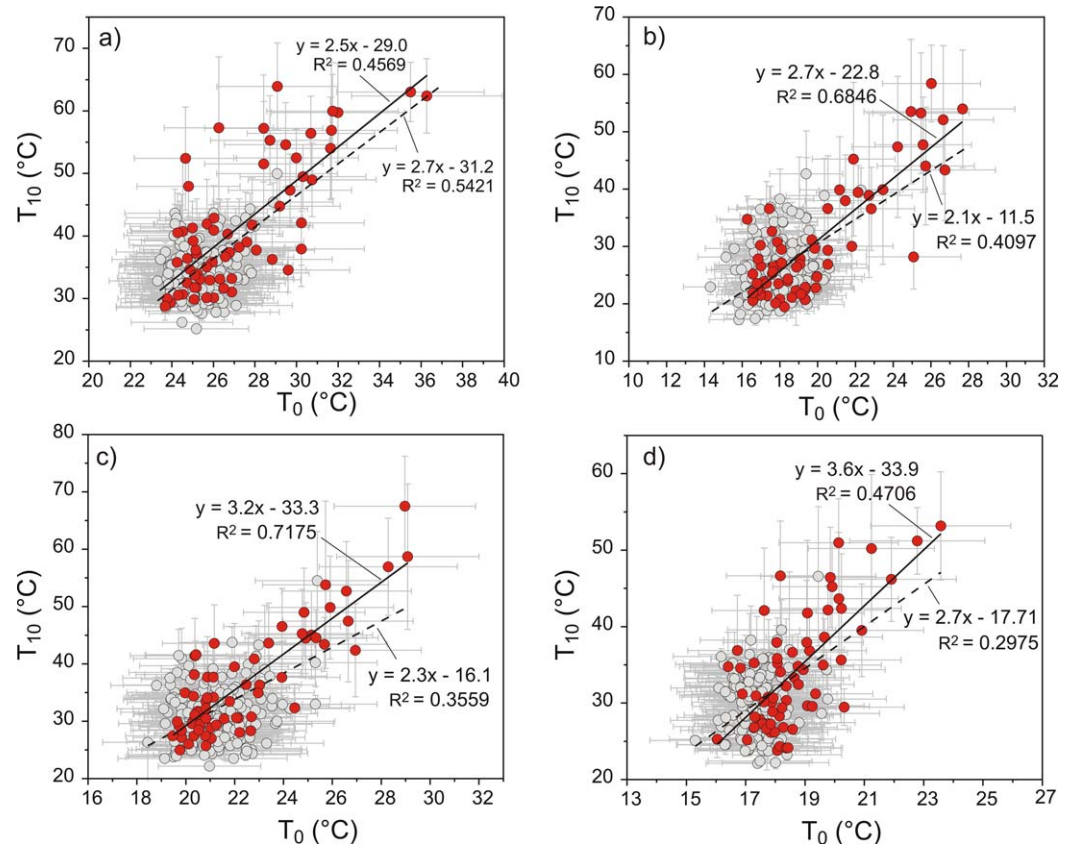
**Figure 6.** Plot of the experimental variogram for T_{10}, T_0, and CO_2 flux n-scores for each survey.

The experimental variogram, $\gamma(h)$, for observations z_i, with $i = 1,,,k$ at locations $x_1,,,x_k$, is defined as:

$$\gamma(h) = \frac{1}{|N(h)|} \sum_{(i,j) \in N(h)} (z_i - z_j)^2 \tag{1}$$

where N(h) denotes the set of pairs of observations i, j such that $|x_i - x_j| = h$, and $|N(h)|$ is the number of pairs in the set. The variogram provides a description of how the data are related (correlated) with distance, in particular the behavior of $\gamma(h)$ with the increase of h describes the spatial pattern of an attribute. The variogram models are given in terms of nugget, sill, and range parameters: the nugget represents the small-scale variation and/or the measurement error and it is estimated from the experimental variogram at h = 0, the sill is the plateau the variogram reaches for a distance equal to the range, which represents the distance at which data are no longer correlated.

In this work, the simulations of CO_2 flux and T_{10} were performed for an area of about 1.45×10^6 m² (Figure 4) considering a simulation grid cell of 10×10 m². For each data set, 100 realizations were processed obtaining the "expected" value at any location, through a pointwise linear average of all the realizations [*Cardellini et al.*, 2003]. The maps of the expected value drawn for a 10×10 m² are reported as supporting information.

Successively, the soil CO_2 flux and T_{10} simulated with sGs on a grid 10 m spaced were reprocessed to estimate the two parameters according to a 90 m spaced grid (cell size 90×90 m²), which correspond to the ground resolution of the ASTER. The soil CO_2 flux and T_{10} were computed for each node as the average of the simulated values falling in a 90×90 m² squared area centered in the grid node. In this way, the computed T_{10} and CO_2 flux estimates and T_0 refer to the same position and have the same footprint. For each average T_{10} and CO_2 flux, the corresponding standard deviations were computed also.
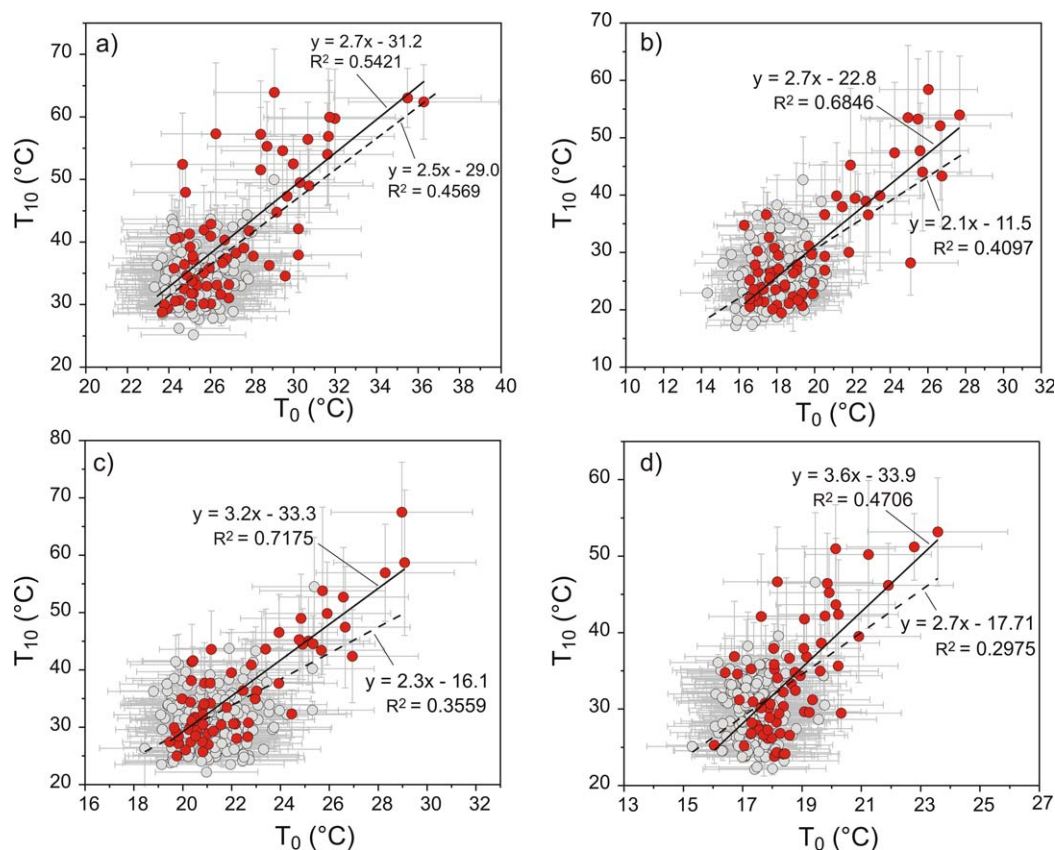
Figure 7. Comparison between T_{10} and T_0. (a) July 2003, (b) May 2010, (c) June 2014, (d) September 2014. The grey dots refer to the entire data set while red dots refer to the values from the Solfatara crater area (box reported in Figure 5); the regression lines computed from the entire data sets and the data subset of Solfatara crater area are reported as dashed lines and continuous lines, respectively. Error bars refer to (i) the uncertainty in T_0 estimate by TES and (ii) to the standard deviation of the estimate average T_{10} (see text for details).

4. Results: Comparison Between Satellite and Ground-Based Measurements

The maps obtained from measured CO_2 fluxes and T_{10} are shown in Figure 5, where the maps of the surface temperature (T_0) derived from the ASTER data for the same area are also reported.

By inspection of the maps, it is evident that CO_2 fluxes and T_{10} values highlight the presence of a fairly well-defined anomaly characterized by the highest flux and temperatures values, for all the periods investigated. This anomaly includes the area inside the Solfatara crater, a NW-SE band corresponding to the Pisciarelli degassing area, and a third area located south of Pisciarelli and SE with respect to the crater. This anomaly corresponds to that defined Solfatara degassing structure (Solfatara DDS) by *Chiodini et al.* [2001] and outlines the strong relation between the degassing process and the heating of the soil [*Chiodini et al.*, 2001, 2005; *Vilardo et al.*, 2015] at Solfatara of Pozzuoli.

Comparing the maps obtained by ground-based measurement with those of T_0 (Figure 5), it is worth noting that all the maps identify the same anomalies. This correspondence suggests that ASTER data are suitable to use for investigating the thermal anomaly.
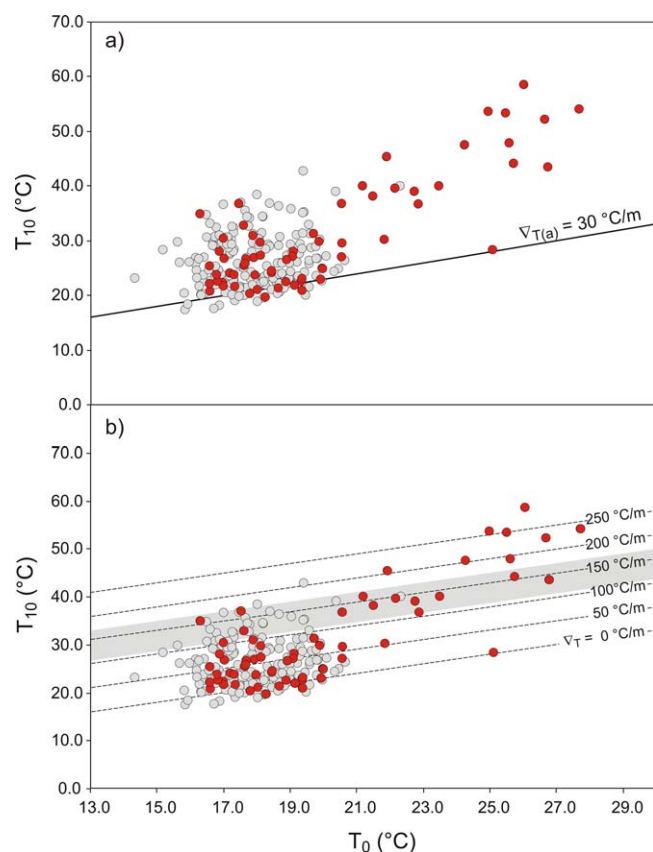
To better characterize and compare the spatial distribution of the different parameters, the variograms (γ) of CO_2 flux, T_{10} and T_0 (Figure 6) were computed considering the data estimated for the 90 m-spaced grid reported in the maps of Figure 5. In order to compare the different variables in the same plot, the variograms of the n-scores of the variables computed by the above described *nscore* algorithm [*Deutsch and Journel*, 1998] are compared in Figure 6. The three variables (CO_2 flux, T_{10}, and T_0) in the four different periods have very similar variograms (Figure 6) all of which can be modeled with a spherical model characterized by similar low nugget values and ranges from 350 to 400 m. Considering that the nugget describes the short-scale variability while the range (i.e., the value of the distance after which the variogram remains

nearly constant) is an estimate of the average size of the anomaly, the similitude shown in Figure 6 demonstrates that the ASTER-derived T_0 refers to the same structure highlighted by high CO_2 flux and soil temperature T_{10}. In other terms, the similarity between the variograms of CO_2 flux, T_{10} and T_0 quantitatively supports the correspondence between soil temperatures, surface temperatures, and CO_2 fluxes highlighted by the maps of Figure 5.

The correlation between ground measurements and ASTER-derived temperatures has been further investigated by a point to point comparison (Figures 7 and 9) of the cell data of Figure 5.

The results show significant correlations between ASTER-derived temperatures (T_0) and soil temperature at 10 cm depth derived from ground measurement (T_{10}) (Figure 7). The correlation is enhanced when referring to the most anomalous areas located in the Solfatara crater (box reported in Figure 5a, red points in Figure 7). In fact the coefficients of determination (R^2) of the linear regressions of T_0-T_{10} sensibly increase, for all the data sets, when the data subsets are considered (Figure 7). Furthermore, Figure 7 shows that T_{10} is systematically higher than T_0. In principle, this deviation can be due (i) to the difference in the time of the measurement (diurnal and nocturnal respectively), (ii) to the occurrence of high thermal gradients (∇_T) in the hottest zones causing a significant temperature increase also at a depth of 10 cm, and (iii) to some systematic biases on the derivation of ASTER temperatures.

In order to investigate this matter, we consider for example the data of May 2010. Figure 8a shows that also at low temperature, T_{10} is always higher than T_0 indicating an apparent thermal gradients of $\sim$30°C m^{-1}. However, because in the low temperature zones of the surveyed area the soil temperature should be affected only by seasonal and diurnal effects and because in these low temperature zones, where diffuse degassing of volcanic gas is absent, the effect of the geothermal gradient due to the conductive heat transfer (i.e., in the order of $10^{-2}-10^{-1}$°C m^{-1}) is negligible, we assume that this $T_{10} - T_0$ difference is likely reflecting the effects of diurnal-nocturnal acquisition of the data (i.e., T_{10} is a diurnal temperature while T_0 is nocturnal). Accordingly, we assume that this apparent thermal gradient of $\sim$30°C m^{-1} on average affects each measurement. In Figure 8b, the T_{10} and T_0 values are compared with different curves of apparent thermal gradients, $\nabla_{T(a)} = \nabla_T + 30$, where ∇_T is the effective thermal gradient. Many data, and in particular those of the higher temperature zones, match the field corresponding to the average thermal gradients (from 107°C m^{-1} to 170°C m^{-1}, grey band in Figure 8b) measured during several campaigns within the hot zones of Solfatara crater [*Chiodini et al.*, 2005]. This finding suggests that the temperature values derived from ASTER, which show a reliable spatial pattern, are also a good proxy of the real surface temperature values.

**Figure 8.** Comparison between T_0 and T_{10} from the May 2010 surveys; in (a) the line corresponding to a thermal gradient of 30°C m^{-1} is reported as a solid line; in (b) the apparent thermal gradient ($\nabla_{T(a)}$) lines, computed for effective thermal gradient (∇_T) from 0°C m^{-1} to 250°C m^{-1}, are reported as dashed lines (see text for details). The grey band corresponds to average measured thermal gradients from 107°C m^{-1} to 170°C m^{-1}, characterizing the hot zones of Solfatara crater [*Chiodini et al.*, 2005]. Color of the points has the same meaning as in Figure 7.

Furthermore, this positive result and the estimated uncertainties on T_0
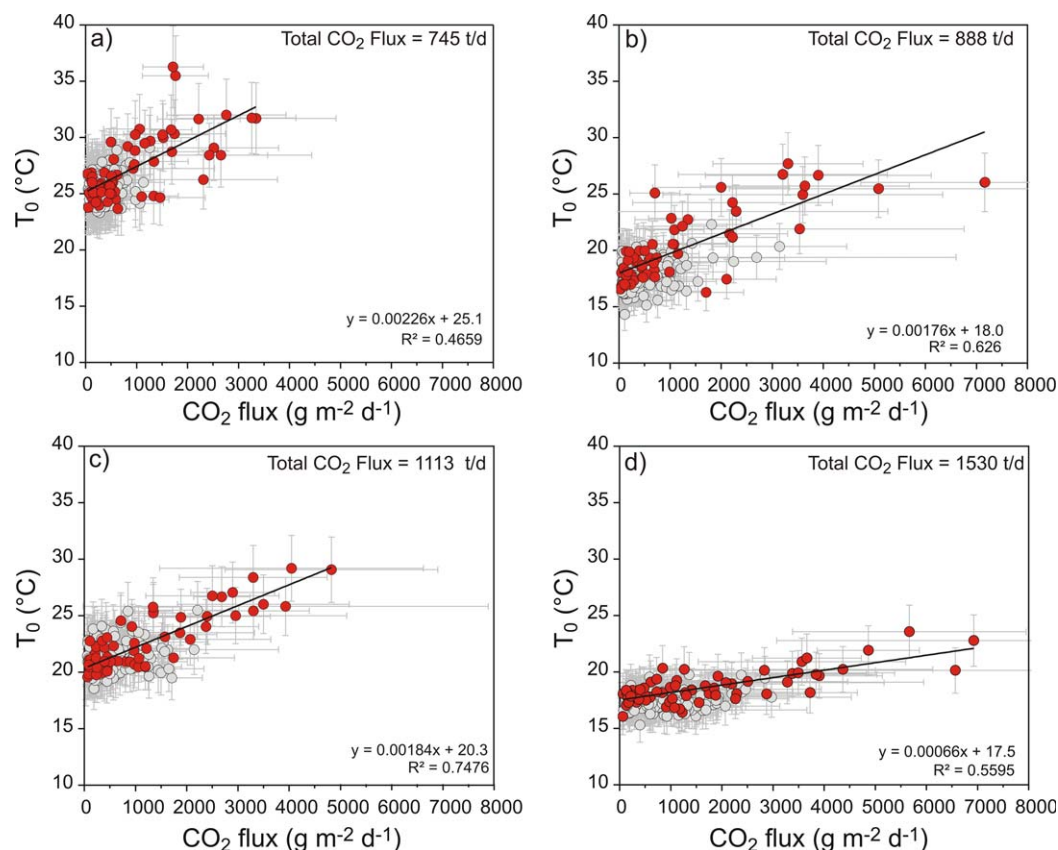
Figure 9. Comparison between CO_2 flux and ASTER-derived surface temperature (T_0). (a) July 2003, (b) May 2010, (c) June 2014, (d) September 2014. Error bars refers to (i) the uncertainty in T_0 estimate by TES and (ii) to the standard deviation of the estimate average CO_2 fluxes (see text for details). The total CO_2 flux released by soil diffuse degassing, computed form for each survey by the measured CO_2 fluxes [*Cardellini et al.*, 2003], is reported in the top right corner of each diagram. Color of the points has the same meaning as in Figure 7.

suggest that difference between T_{10} and T_0 is only for a minor extent caused by systematic errors due to the methodology for obtaining ASTER-derived temperature.

ASTER-estimated T_0 well correlates also with estimated average CO_2 fluxes for all the considered data set (Figure 9). Considering that background CO_2 fluxes are typically orders of magnitude lower than the anomalous one, the intercept of the regression lines in the new plots CO_2 flux versus T_0 of Figure 9 (i.e., the T_0 value for null CO_2 flux) are a good proxy of the background temperature, i.e., the surface soil temperature where a CO_2 flux from the hydrothermal system is absent. The intercepts, in fact, correspond to surface temperatures 25.1, 18.0, 23.4, and 17.5°C for the surveys of July 2003, May 2005, June 2014, and September 2014, respectively, which are consistent with the ambient temperatures of the different seasons. The slopes of the regression lines, instead, seem to be controlled mainly by the total amount of CO_2 released, in fact, the slope values generally decrease with the increase of the total CO_2 flux (Figure 9).

In general the correlation of soil temperature (both T_{10} and T_0) and CO_2 flux confirms that the hot soils of the area are heated by the subsoil condensation of the steam rising from the hydrothermal system, a process which at the same time supplies CO_2 and heat generating hot and high gas flux soils [*Chiodini et al.*, 2001, 2005].

5. Conclusions and Perspectives

The surface temperatures derived from ASTER data analysis are compared with a large data set of soil temperature and CO_2 fluxes measured in a volcanic-hydrothermal system, the Solfatara of Pozzuoli. The spatial distribution of ASTER-derived surface temperatures are in good agreement with that derived by in situ measurements suggesting that the remote survey of surface temperature is a suitable and powerful tool to

investigate hydrothermal features. The correspondence between temperatures and CO_2 flux distributions indicates that the soil thermal anomaly is due to the arrival at the surface of fumarolic-type fluids which undergo subterranean condensation of the steam, a process which heats the soils and simultaneously feeds CO_2 soil degassing [*Chiodini et al.*, 2001, 2005].

A "point-to-point" comparison between remotely sensed and measured temperatures, acquired in four different surveys, shows a reasonably good linear correlation between the two parameters. In general, remotely sensed temperatures result systematically lower than measured ones, the latter being measured at a depth of 10 cm and hence increased by high thermal gradients of the soil in the hottest zones. In fact, the differences between remotely sensed surface temperatures and those measured in the soil, once corrected for diurnal-nocturnal effects, are compatible with average thermal gradients of 107–170°C/m characterizing Solfatara crater [*Chiodini et al.*, 2005].

Due the good correlation between remotely sensed temperatures and measured CO_2 fluxes, the comparison of these two parameters turned out to be a good tool to estimate the background temperature, i.e., the surface temperature where a CO_2 flux from the hydrothermal system is absent and therefore it absent the heating due to the degassing process. Furthermore, for the four investigated periods, the correlation between surface temperature seems to be linked to the total amount of CO_2 released by soil degassing.

The results of this study demonstrate that satellite data can be a very powerful tool to study surface thermal anomalies quantitatively. In principle, the thermal release of any active volcanoes can be remotely monitored with proper frequency and spatial resolution. Thanks to its high-spatial resolution, ASTER offers the capability to measure thermal characteristics also in small areas like Solfatara of Pozzuoli. A further improvement in the use of satellite data could derive from increasing, in future missions with TIR instruments, the spatial resolutions ($<$100 m/pixel), and the temporal sampling. Furthermore, the long data set already acquired by satellites, represents an invaluable resource to investigate the thermal history of active volcanoes and, in particular, of those that recently erupted. At Campi Flegrei, where an ongoing heating process has been highlighted by classical monitoring techniques, the satellite data can provide a supplemental tool to monitor the thermal evolution of this dangerous area.

References

Acocella, V., and G. Chiodini (2015), Better Forecasting for the Next Volcanic Eruption, *EOS*, *96*, doi:10.1029/2015EO039135.

Aiuppa, A., G. Tamburello, R. Di Napoli, C. Cardellini, G. Chiodini, G. Giudice, F. Grassa, and M. Pedone (2013), First observations of the fumarolic gas output from a restless caldera: Implications for the current period of unrest (2005–2013) at Campi Flegrei, *Geochem. Geophys. Geosyst.*, *14*, 4153–4169, doi:10.1002/ggge.20261.

Aiuppa, A., L. Fiorani, S. Santoro, S. Parracino, M. Nuvoli, G. Chiodini, C. Minopoli, and G. Tamburello (2015), New ground-based lidar enables volcanic CO_2 flux measurements, *Sci. Rep.*, *5*, 13614, doi:10.1038/srep13614.

Bergfeld, D., W. C. Evans, J. B. Lowenstern, and S. Hurwitz (2012), Carbon dioxide and hydrogen sulfide degassing and cryptic thermal input to Brimstone Basin, Yellowstone National Park, Wyoming, *Chem. Geol.*, *330–331*, 233–243.

Blackett, M. (2013), Review of the utility of infrared remote sensing for detecting and monitoring volcanic activity with the case study of shortwave infrared data for lascar volcano from 2001–2005, in *Remote Sensing of Volcanoes and Volcanic Processes: Integrating Observation and Modelling, Spec. Publ. 380*, edited by D. M. Pyle, T. A. Mather, and J. Biggs, pp. 107–135, Geol. Soc. London, London, U. K.

Bloomberg, S., C. Werner, C. Rissmann, A. Mazot, T. Horton, D. Gravley, B. Kennedy, and C. Oze (2014), Soil CO_2 emissions as a proxy for heat and mass flow assessment, Taupō Volcanic Zone, New Zealand, *Geochem. Geophys. Geosyst.*, *15*, 4885–4904, doi:10.1002/2014GC005327.

Buongiorno, M. F., et al. (2008), Etna 2003 field campaign: Calibration and validation of paceborne and airborne instruments for volcanic applications, *ASI projects: I/R/157/02, I/R/203/02, Quaderni di Geofisica, INGV*, *56*, 1–90.

Buongiorno, M. F., D. C. Pieri, and M. Silvestri (2013), Thermal analysis of volcanoes based on 10 years of ASTER data on Mt. Etna, in *Thermal Infrared Remote Sensing: Sensors, Methods, Applications, Remote Sensing and Digital Image Processing*, edited by C. Kuenzer and S. Dech, vol. 17, pp. 409–428, doi:10.1007/978-94-007-6639-6_20.

Caliro, S., G. Chiodini, D. Galluzzo, D. Granieri, M. La Rocca, G. Saccorotti, and G. Ventura (2005), Recent activity of Nisyros volcano (Greece) inferred from structural, geochemical and seismological data, *Bull. Volcanol.*, *67*, 358–369, doi:10.1007/s00445-004-0381-7.

Cardellini, C., G. Chiodini, and G. Frondini (2003), Application of stochastic simulation to CO_2 flux from soil: Mapping and quantification of gas release, *J. Geophys. Res.*, *108*(B9), 2425, doi:10.1029/2002JB002165.

Carter, A. J., and M. S. Ramsey (2009), ASTER- and field-based observations at Bezymianny Volcano: Focus on the 11 May 2007 pyroclastic flow deposit, *Remote Sens. Environ.*, *113*, 2142–2151.

Carter, A. J., M. S. Ramsey, A. J. Durant, I. P. Skilling, and A. L. Wolfe (2009), Micron-scale roughness of volcanic surfaces from thermal infrared spectroscopy and scanning electron microscopy, *J. Geophys. Res.*, *114*, B02213, doi:10.1029/2008JB005632.

Chiodini, G., F. Frondini, and B. Raco (1996), Diffuse emission of CO_2 from the Fossa crater, Vulcano Island (Italy), *Bull. Volcanol.*, *58*, 41–50.

Chiodini, G., R. Cioni, M. Guidi, B. Raco, and L. Marini (1998), Soil CO2 flux measurements in volcanic and geothermal areas, *Appl. Geochem.*, *13*(5), 543–552.

Chiodini, G., F. Frondini, C. Cardellini, D. Granieri, L. Marini, and G. Ventura (2001), CO_2 degassing and energy release at Solfatara volcano, Campi Flegrei, Italy, *J. Geophys. Res.*, *106*, 16,213–16,221, doi:10.1029/2001JB000246.

Chiodini, G., D. Granieri, R. Avino, S. Caliro, A. Costa, and C. Werner (2005), Carbon dioxide diffuse degassing and estimation of heat release from volcanic and hydrothermal systems, *J. Geophys. Res.*, *110*, B08204, doi:10.1029/2004JB003542.

Chiodini, G., G. Vilardo, V. Augusti, D. Granieri, S. Caliro, C. Minopoli, C. Terranova (2007), Thermal monitoring of hydrothermal activity by permanent infrared automatic stations. Results obtained at Solfatara di Pozzuoli, Campi Flegrei (Italy), *J. Geophys. Res.*, *112*, B12206, doi: 10.1029/2007JB005140.

Chiodini, G., S. Caliro, C. Cardellini, D. Granieri, R. Avino, A. Baldini, M. Donnini, and C. Minopoli (2010), Long-term variations of the Campi Flegrei, Italy, volcanic system as revealed by the monitoring of hydrothermal activity, *J. Geophys. Res.*, *115*, B03205, doi:10.1029/2008JB006258.

Chiodini, G., S. Caliro, P. De Martino, R. Avino, and F. Gherardi (2012), Early signals of new volcanic unrest at Campi Flegrei caldera? Insights from geochemical data and physical simulations, *Geology*, *40*, 943–946, doi:10.1130/G33251.1.

Chiodini, G., J. Vandemeulebrouck, S. Caliro, L. D'Auria, P. De Martino, A. Mangiacapra, and Z. Petrillo (2015), Evidence of thermal-driven processes triggering the 2005–2014 unrest at Campi Flegrei caldera, *Earth Planet. Sci. Lett.*, *414*, 58–67, doi:10.1016/j.epsl.2015.01.012.

Coppola, D., M. R. James, T. Staudacher, and C. Cigolini (2010), A comparison of field- and satellite-derived thermal flux at Piton de la Fournaise: Implications for the calculation of lava discharge rate, *Bull. Volcanol.*, *72*(3), 341–356.

Costa, A., V. C. Smith, G. Macedonio, and N. E. Matthews (2014), The magnitude and impact of the Youngest Toba Tuff super-eruption, *Front. Earth. Sci.*, *2*, 1–8, doi:10.3389/feart.2014.00016.

Davies, A.G., J. Calkins, L. Scharenbroich, R.G. Vaughan, R. Wright, P. Kyle, R. Castaño, S. Chien, and D. Tran (2008), Multi-instrument Remote and in situ Observations of the Erebus Volcano (Antarctica) Lava Lake in 2005: A Comparison with the Pele Lava Lake on the Jovian Moon Io, *J. Volcanol. Geotherm. Res.*, *177*(3), 705–724.

De Bono, A, G. Giuliani, S. Kluser, and P. Peduzzi (2004), Impacts of Summer 2003 Heat Wave in Europe, *UNEP/DEWA/GRID-Europe Environment Alert Bulletin*, *2*, 1–4.

Deino, A. L., G. Orsi, S. De Vita, and M. Piochi (2004), The age of the Neapolitan Yellow Tuff caldera-forming eruption (Campi Flegrei caldera—Italy) assessed by ^{40}Ar/^{39}Ar dating method, *J. Volcanol. Geotherm. Res.*, *133*, 157–70.

Del Gaudio, C., I. Aquino, G. P. Ricciardi, C. Ricco, and R. Scandone (2010), Unrest episodes at Campi Flegrei: A reconstruction of vertical ground movements during 1905–2009, *J. Volcanol. Geotherm. Res.*, *195*(1), 48–56, doi:10.1016/j.jvolgeores.2010.05.014.

Deutsch, C. V., and A. G. Journel (1998), *GSLIB: Geostatistical Software Library and Users Guide*, 369 pp., Oxford Univ. Press, N. Y.

Flynn, L. P., P. J. Mouginis-Mark, and K. A. Horton (1994), Distribution of thermal areas on active lava flow field: Landsat observations of Kilauea, Hawaii, July 1991, *Bull. Volcanol.*, *56*, 284–296.

Francis, X.V., C. Chemel, R.S. Sokhi, E. G. Norton, H.M.A. Ricketts, and B.E.A. Fisher (2011), Mechanisms responsible for the build-up of ozone over South East England during the August 2003 heatwave, *Atmos. Environ.*, *45*, 6880–6890, doi:10.1016/j.atmosenv.2011.04.035.

Gillespie, A., S. Rokugawa, T. Matsunaga, J. S. Cothern, S. J. Hook, and A. B. Kahle (1998), A temperature and emissivity separation algorithm for Advanced Spaceborne Thermal Emission and Reflection Radiometer (ASTER) images, *IEEE Trans. Geosci. Remote Sens.*, *36*(4), 1113–1126.

Goovaerts, P. (1997), *Geostatistics for Natural Resources Evaluation*, Oxford Univ. Press, N. Y.

Harris, A. J. L., and D. S. Stevenson (1997), Thermal observations of degassing open conduits and fumaroles at Stromboli and Vulcano using remotely sensed data, *J. Volcanol. Geotherm. Res.*, *76*, 175–198.

Harris, A. J. L., L. P. Flynn, L. Keszthelyi, P. J. Mouginis-Mark, S. K. Rowland, and J. A. Resing (1998), Calculation of lava effusion rates from Landsat TM data, *Bull. Volcanol.*, *60*, 52−71.

Harvey, M. C., J. V. Rowland, G. Chiodini, C. F. Rissmann, S. Bloomberg, P. A. Hernández, A. Mazot, F. Viveiros, and C. Werner (2015), Heat flux from magmatic hydrothermal systems related to availability of fluid recharge, *J. Volcanol. Geotherm. Res.*, *302*, 225–236, doi: 10.1016/j.jvolgeores.2015.07.003.

Hirn, B., C. Di Bartola, G. Laneve, E. Cadau, and F. Ferrucci (2008), SEVIRI onboard Meteosat Second Generation, and the quantitative monitoring of effusive volcanoes in Europe and Africa, *Proceedings IGARSS 2008*, 8–11 July, 374–377, Boston, Mass., doi:10.1109/IGARSS.2008.4779361.

Hurwitz, S., R. N. Harris, C. A. Werner, and F. Murphy (2012), Heat flow in vapor dominated areas of the Yellowstone Plateau volcanic field: Implications for the thermal budget of the Yellowstone Caldera, *J. Geophys. Res.*, *117*, B10207, doi:10.1029/2012JB009463.

Isaaks, E. H., and R. M. Srivastava (1989), *An Introduction to Applied Geostatistics*, 561 pp., Oxford Univ. Press, N. Y.

Kahle, A. B., F. D. Palluconi, S. J. Hook, V. J. Realmuto, and G. Bothwell (1991), The Advanced Spaceborne Thermal Emission and Reflectance Radiometer (ASTER), *Int. J. Imag. Syst. Technol.*, *3*, 144–156.

Kaneko, T., M. J. Wooster, and S. Nakada (2002), Exogenous and endogenous growth of the Unzen lava dome examined by satellite infrared image analysis, *J. Volcanol. Geotherm. Res.*, *116*, 151–160.

Kervyn, M., G. G. J. Ernst, A. Harris, E. Mbede, F. Belton, and P. Jacobs (2008), Thermal remote sensing of the low-intensity carbonatite volcanism of Oldoinyo Lengai, Tanzania, *Int. J. Remote Sens.*, *29*, 6467–6499.

Lagios, E., S. Vassilopoulou, V. Sakkas, V. Dietrich, B. N. Damiata, and A. Ganas (2007), Testing satellite and ground thermal imaging of low-temperature fumarolic fields: The dormant Nisyros Volcano (Greece), *ISPRS J. Photogramm. Remote Sens.*, *62*, 447–460.

Lombardo, V., M. F. Buongiorno, L. Merucci, and D. C. Pieri (2004), Differences in Landsat TM derived lava flow thermal structure during summit and flank eruption at Mount Etna, *J. Volcanol. Geotherm. Res.*, *134*(1–2), 15–34.

Musacchio, M., S. Amici, M. Silvestri, S. Teggi, M. F. Buongiorno, S. Silenzi, and S. Devoti (2007), Application of CIRILLO a new atmospheric correction tool on Castel Porziano Beach (CPB), Proc. SPIE 6749, Remote Sensing for Environmental Monitoring, GIS Applications, and Geology VII, 674935 (October 30), doi:10.1117/12.752670.

Oppenheimer, C. (1993), Infrared surveillance of crater lakes using satellite data, *J. Volcanol. Geotherm. Res.*, *55*, 117–128.

Oppenheimer, C. (1998), Volcanological applications of meteorological satellites, *Int. J. Remote Sens.*, *19*, 2829–2864.

Oppenheimer, C., and G. Yirgu (2002), Thermal imaging of an active lava lake: Erta 'Ale volcano, Ethiopia, *Int. J. Remote Sens.*, *23*(22), 4777–4782.

Pedone, M., A. Aiuppa, G. Giudice, F. Grassa, C. Cardellini, G. Chiodini, and M. Valenza (2014), Volcanic CO_2 flux measurement at Campi Flegrei by tunable diode laser absorption spectroscopy, *Bull. Volcanol.*, *76*, 812, doi:10.1007/s00445-014-0812-z.

Pieri, D., and M. Abrams (2005), ASTER Observations of thermal precursors to the April 2003 Eruption of Chikurachki Volcano, Kurile Islands, Russia, *Remote Sens. Environ.*, *99*, 84–94.

Ramsey, M. S. (2002), Ejecta distribution patterns at Meteor Crater, Arizona: On the applicability of lithologic end-member deconvolution for spaceborne thermal infrared data of Earth and Mars, *J. Geophys. Res.*, *107*(E8), 5059, doi:10.1029/2001JE001827.

Ramsey, M. S., and J. Dehn (2004), Spaceborne observations of the 2000 Bezymianny, Kamchatka eruption: The integration of high-resolution ASTER data into near real-time monitoring using AVHRR, *J. Volcanol. Geotherm. Res.*, *135*(1–2), 127–146, doi:10.1016/j.jvolgeores.2003.12.014.

Trunk, L., and A. Bernard (2008), Investigating crater lake warming Using ASTER thermal imagery: Case studies at Ruapehu, Poás, Kawah Ijen, and Copahué Volcanoes, *J. Volcanol. Geotherm. Res.*, *178*, 259–270.

Vaughan, R. G., and S. J. Hook (2006), Using Satellite Data to Characterize the Temporal Thermal Behavior of an Active Volcano: Mount St. Helens, WA, *Geophys. Res. Lett.*, *33*, L20303, doi:10.1029/2006GL027957.

Vaughan, R. G., L. P. Keszthelyi, A. G. Davies, D. J. Schneider, C. Jaworowski, and H. Heasler (2010), Exploring the Limits of Identifying Sub-pixel Thermal Features using ASTER TIR Data, *J. Volcanol. Geotherm. Res.*, *189*(3–4), 225–237, doi:10.1016/j.jvolgeores.2009.11.010.

Vaughan, R. G., L. P. Keszthelyi, J. B. Lowenstern, C. Jaworowski, and H. Heasler (2012a), Use of ASTER and MODIS thermal infrared data to quantify heat flow and hydrothermal change at Yellowstone National Park, *J. Volcanol. Geotherm. Res.*, *233-234*, 72–89, doi:10.1016/j.jvolgeores.2012.04.022.

Vaughan, R. G., J. B. Lowenstern, L. P. Keszthelyi, C. Jaworowski, and H. Heasler (2012b), Mapping Temperature and Radiant Geothermal Heat Flux Anomalies in the Yellowstone Geothermal System Using ASTER Thermal Infrared Data, *GRC Trans.*, *36*, 1403–1410.

Vilardo, G., F. Sansivero, and G. Chiodini (2015), Long-term TIR imagery processing for spatiotemporal monitoring of surface thermal features in volcanic environment: A case study in the Campi Flegrei (Southern Italy), *J. Geophys. Res. Solid Earth*, *120*, 812–826, doi:10.1002/2014JB011497.

Wright, R., and E. Pilger (2008), Satellite observations reveal little inter-annual variability in the radiant flux from the Mount Erebus lava lake, *J. Volcanol. Geotherm. Res.*, *177*(3), 687–694.

Yamaguchi, Y., A. B. Kahle, H. Tsu, T. Kawakami, and M. Pniel (1998), Overview of Advanced Spaceborne Thermal Emission and Reflection Radiometer (ASTER), *IEEE Trans. Geosci. Remote Sens.*, *36*, 1062–1071.